Design criteria for a beam-driven resonant passive transverse deflector for longitudinal beam diagnostics

Dmitry Bazyl,* Winfried Decking, Sergey Tomin, and Igor Zagorodnov
Deutsches Elektronen-Synchrotron DESY, Notkestrasse 85, 22607, Hamburg, Germany

(Received 23 June 2026; accepted 21 October 2026; published 5 November 2026)

Conventional radio-frequency (rf) transverse deflecting structures provide high-resolution longitudinal beam diagnostics, but require externally generated high-power rf, waveguide distribution, synchronization, and input coupling at the operating frequency. We propose design criteria for a beam-driven resonant passive transverse deflector that does not require an external rf source. A leading drive bunch excites long-range wakefields in an off-axis periodic copper structure and a delayed witness bunch experiences the transverse wake near a zero crossing. The concept is based on the large temporal slope available from high-frequency wake components. A structure designed for installation after the second bunch compressor in the three-bunch-compressor layout of the European XFEL is optimized to place the zero crossing of the drive-bunch-induced transverse wake potential approximately one rf-bucket spacing of the 1.3 GHz linac behind the drive bunch. The selected geometry produces a multimode transverse kick dominated by TM-like modes. We use time-domain wake simulations, frequency-domain decomposition, cell-number scaling, mechanical-tolerance scans, orbit-offset studies, and uniform thermal scaling to determine the operating point and its sensitivity. For this geometry, the zero crossing occurs at $s_0 \simeq 230.6$ mm, with a per-cell temporal slope of $S_{\mathrm{cell}} = 1.186\ \mathrm{mV}/(\mathrm{pC\,fs\,cell})$. For a compact 1 m structure operated with a 250 pC drive bunch and a 700 MeV witness beam, the estimated temporal resolution is about 33 fs.

DOI: 10.1103/g8fg-s5pd

I. INTRODUCTION

State-of-the-art high-power radio-frequency (rf) transverse deflecting cavities are widely used for electron-beam diagnostics [1–10]. Such cavities are operated in externally driven dipole modes and require high-power rf infrastructure and stable synchronization. In contrast, the method proposed in Ref. [11] relies on beam-induced resonant electromagnetic fields (wakefields) and does not require externally supplied high-power rf. In this concept, a leading drive bunch excites resonant fields in a periodic iris-loaded copper rf structure. A delayed witness bunch samples the corresponding transverse kick. In general, the drive bunch excites a spectrum of resonant modes, with high-frequency components suppressed by the bunch form factor. Through geometric optimization, the modal contributions can be phased such that they add constructively at the witness-bunch delay. The effective streaking voltage increases approximately linearly with the number of periods in the deflecting structure over the range considered here.

*Contact author: dmitry.bazyl@desy.de

Published by the American Physical Society under the terms of the Creative Commons Attribution 4.0 International license. Further distribution of this work must maintain attribution to the author(s) and the published article's title, journal citation, and DOI.

The proposed beam-driven transverse deflecting structure is closely related to earlier work on passive wakefield streaking and plasma-wakefield diagnostics. Passive corrugated or dechirper-based structures [12] have used self-induced short-range wakefields to correlate longitudinal position with transverse kick [13–16]. In plasma-based diagnostics, laser-driven plasma wakes have been proposed as attosecond streaking fields, while drive-probe experiments have measured transverse plasma wakefields excited by an off-axis leading bunch and sampled by a trailing witness bunch [17,18]. Related high-frequency deflector work by Dolgashev and collaborators includes W-band and millimeter-wave structures in which beam-driven fields and deflecting gradients were studied [19,20]. The distinguishing feature of the proposed resonant approach is the use of sufficiently long-lived resonant wakefields excited by a preceding drive bunch, allowing a delayed witness bunch to sample an approximately linear zero-crossing kick. In this sense, the structure acts as a passive analogue of an rf transverse deflector.

The following sections develop the modal design criterion and apply it to a finite off-axis copper structure. We first define the zero-crossing operating point, the spatial and temporal wake slopes, and the modal overlap quantities. The closed-pillbox model is then used to estimate the offset and aperture dependence of the dominant TM-like modes. Time-domain wake simulations are

used to determine the optimized geometry, the per-cell slope, the cell-number scaling, and the harmonic content of the wake derivative. Mechanical, orbit and temperature sensitivity studies quantify the stability of the operating point, while a low-energy European XFEL example illustrates its practical implementation for beam diagnostics.

II. MODAL PRINCIPLE AND DESIGN CRITERIA

Consider a drive bunch of charge q_d travelling with velocity $v \simeq c$ through a periodic N-cell passive deflecting structure, shown schematically in Fig. 1. The structure is characterized by the cell period P, pillbox radius R, cell length L_c, beam-pipe diameter d_{pipe}, and transverse pipe-offset vector $\boldsymbol{\rho}$ measured from the pillbox axis to the beam-pipe axis. A witness bunch follows the drive bunch at a longitudinal distance $s > 0$. The transverse positions of the source (drive) and witness bunches are denoted by $\mathbf{r}_s$ and $\mathbf{r}_w$, respectively. The same-trajectory case used for the design formulas is obtained by setting $\mathbf{r}_s = \mathbf{r}_w = \mathbf{r}_b$; for the nominal design trajectory, $\mathbf{r}_b = \boldsymbol{\rho}$.

The coordinate system is right-handed, with z along the nominal bunch trajectory, x in the horizontal plane, and y in the vertical plane. The distance s denotes the drive-witness separation: a field left behind by the drive bunch is sampled by the witness at time $t = (z + s)/c$. The wake potentials are defined using the standard convention for relativistic beams [21–23]. The longitudinal wake potential per unit drive charge is defined as

$$W_{\parallel}(\mathbf{r}_w, \mathbf{r}_s; s) = -\frac{1}{q_d}\int_{\Gamma_w} E_z\left(\mathbf{r}_w, z, t = \frac{z+s}{c}\right) dz, \qquad s > 0. \tag{1}$$

Here, Γ_w is the witness trajectory. With this convention, a positive longitudinal wake corresponds to energy loss of a trailing electron bunch when q_d is understood as the positive charge magnitude of the drive bunch.

The transverse wake potential is defined from the transverse Lorentz voltage per unit drive charge,

$$\mathbf{W}_{\perp}(\mathbf{r}_w, \mathbf{r}_s; s) = \frac{\mathbf{1}}{\boldsymbol{q}_d}\int_{\Gamma_w} [\mathbf{E}_{\perp} + c\hat{\mathbf{z}} \times \mathbf{B}]_{\mathbf{r}_w, z, t=(z+s)/c} dz, \qquad s > 0. \tag{2}$$

The sign of the actual transverse momentum change is obtained by multiplying this voltage by the witness charge. The selected streaking direction is denoted by the transverse unit vector $\mathbf{e}_s$, and the projected transverse wake is

$$W_s(\mathbf{r}_w, \mathbf{r}_s; s) = \mathbf{e}_s \cdot \mathbf{W}_{\perp}(\mathbf{r}_w, \mathbf{r}_s; s). \tag{3}$$

For vertical streaking $\mathbf{e}_s = \hat{\mathbf{y}}$, whereas for horizontal streaking $\mathbf{e}_s = \hat{\mathbf{x}}$. Later, the structure optimization, scaling, and sensitivity studies use the vertical wake. For this case, $W_y \equiv W_s$ and $D_y \equiv D_s$ and the corresponding temporal slope is denoted by S_y.

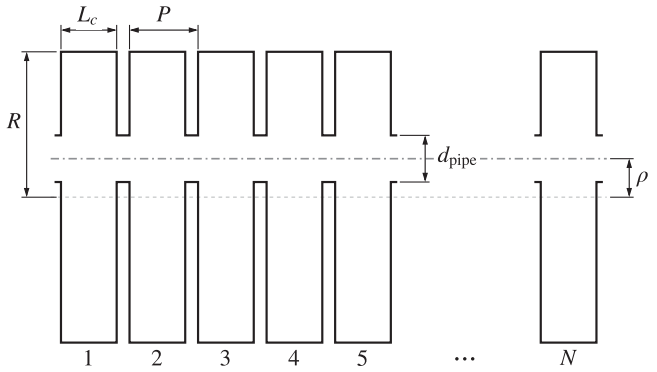


FIG. 1. Schematic longitudinal section of an N-cell off-axis pillbox array. The light dashed line denotes the cylindrical pillbox axis. The darker dash-dotted line denotes the displaced beam trajectory through the beam pipe. The relevant geometric parameters are the pillbox radius R, cell length L_c, period P, beam-pipe diameter d_{pipe}, and transverse offset $\rho = |\boldsymbol{\rho}|$.

The passive deflector is operated near a zero crossing of the long-range transverse wake,

$$W_s(\mathbf{r}_w, \mathbf{r}_s; s_0) \simeq 0, \qquad D_s(\mathbf{r}_w, \mathbf{r}_s; s_0) = \left.\frac{dW_s(\mathbf{r}_w, \mathbf{r}_s; s)}{ds}\right|_{s=s_0}. \tag{4}$$

If the longitudinal coordinate inside the witness bunch is denoted by ζ, measured as an additional delay relative to the reference separation s_0, then

$$W_s(\mathbf{r}_w, \mathbf{r}_s; s_0 + \zeta) = W_s(\mathbf{r}_w, \mathbf{r}_s; s_0) + D_s(\mathbf{r}_w, \mathbf{r}_s; s_0)\zeta + O(\zeta^2). \tag{5}$$

At an exact zero crossing, $W_s(\mathbf{r}_w, \mathbf{r}_s; s_0) = 0$ and the local wake derivative D_s is the passive analogue of the deflecting-voltage slope in an active transverse deflecting rf structure. In this paper, D_s denotes the spatial derivative with respect to the drive-witness separation s. If the corresponding time coordinate is defined by $s = ct$, the temporal streaking slope is

$$S_y(\mathbf{r}_w, \mathbf{r}_s; s_0) = \left.\frac{dW_y(\mathbf{r}_w, \mathbf{r}_s; s)}{dt}\right|_{s=s_0} = cD_y(\mathbf{r}_w, \mathbf{r}_s; s_0). \tag{6}$$

For a relativistic drive and witness bunch, the long-range wake is represented below as a sum over resonant eigenmodes, following the standard wakefield and impedance formalism [21,22]. Such an eigenmode expansion is exact for a closed, lossless perfectly conducting cavity, where the modes form a complete orthogonal set and have real eigenfrequencies. The present structure, however, is

open and may include material or external losses. In this case, the representation by real resonance frequencies and quality factors is an approximation to the more general pole expansion of the impedance.

In the more accurate resonator treatment, the wake is obtained from the complex poles of the impedance. The damping is then accompanied by a shift of the oscillation frequency, as discussed in the standard treatment of resonator wakes and impedances by Chao [21]. In the present work, we neglect this small frequency shift and use the simpler engineering representation in which each relevant resonance is described by a real resonance frequency ω_m and a loaded quality factor Q_m. This approximation is sufficient because the purpose of this section is to formulate the modal design principle and the dominant mode-selection criteria.

We use the field convention $\exp(-i\omega t)$. For mode m, let ω_m be the real angular resonance frequency used in this approximate modal representation, Q_m the corresponding loaded quality factor and

$$k_m = \frac{\omega_m}{c}, \qquad \alpha_m = \frac{\omega_m}{2Q_m c} \tag{7}$$

the synchronous wavenumber and spatial damping constant, respectively.

From this point on, we specialize the working modal formulas to the same-trajectory case, $\mathbf{r}_s = \mathbf{r}_w = \mathbf{r}_b$ and $\Gamma_d = \Gamma_w = \Gamma_b$. The synchronous longitudinal voltage of mode m on this common trajectory is

$$V_{z,m}(\mathbf{r}_b) = \int_{\Gamma_b} E_{z,m}(\mathbf{r}_b, z)\exp(ik_m z)dz. \tag{8}$$

The Gaussian drive-bunch form factor is

$$F_m = \exp\left[-\frac{1}{2}\left(\frac{\omega_m \sigma_z}{c}\right)^2\right], \tag{9}$$

where σ_z is the rms bunch length.

With U_m denoting the stored energy of mode m, the positive longitudinal modal amplitude is defined by the standard same-trajectory cavity-mode loss-factor normalization,

$$K_{\parallel,m}(\mathbf{r}_b) = \frac{|V_{z,m}(\mathbf{r}_b)|^2}{2U_m} F_m. \tag{10}$$

This expression is independent of the arbitrary normalization of the eigenmode fields: the voltages scale linearly with the field amplitude, while the stored energy scales quadratically. In the common higher-order mode convention, $K_{\parallel,m} = 2k_m^{\mathrm{loss}} F_m$. The longitudinal modal wake is then written as

$$W_{\parallel,m}(\mathbf{r}_b; s) = K_{\parallel,m}(\mathbf{r}_b)\exp(-\alpha_m s)\cos(k_m s), \qquad s > 0. \tag{11}$$

The transverse Lorentz voltage of mode m, projected onto the selected streaking direction, is defined by

$$V_{s,m}(\mathbf{r}_b) = \mathbf{e}_s \cdot \int_{\Gamma_b} [\mathbf{E}_{\perp,m} + c\,\hat{\mathbf{z}} \times \mathbf{B}_m](\mathbf{r}_b, z)\exp(ik_m z)dz. \tag{12}$$

The corresponding positive transverse modal amplitude is

$$K_{s,m}(\mathbf{r}_b) = \frac{|V_{z,m}^*(\mathbf{r}_b) V_{s,m}(\mathbf{r}_b)|}{2U_m} F_m. \tag{13}$$

The transverse modal wake in the selected streaking direction is then

$$W_{s,m}(\mathbf{r}_b; s) = K_{s,m}(\mathbf{r}_b)\exp(-\alpha_m s)\sin(k_m s), \qquad s > 0. \tag{14}$$

Thus, the longitudinal wake of a resonant mode has the cosine phase, while the transverse wake has the sine phase.

The phase relation follows from the Panofsky-Wenzel theorem [1,21,23]. With the wake definitions used above,

$$\frac{\partial \mathbf{W}_\perp(\mathbf{r}_w, \mathbf{r}_s; s)}{\partial s} = \nabla_{\perp,w} W_\parallel(\mathbf{r}_w, \mathbf{r}_s; s), \tag{15}$$

where the transverse gradient is taken with respect to the witness position, with the drive position held fixed. In the same-trajectory specialization, $\mathbf{r}_w = \mathbf{r}_s = \mathbf{r}_b$ is imposed only after this gradient is evaluated. For the same harmonic convention, after this order of operations is applied, the corresponding voltage relation can be written, apart from end-point terms, as

$$\mathbf{V}_{\perp,m}(\mathbf{r}_b) = \frac{i}{k_m} \nabla_\perp V_{z,m}(\mathbf{r}_b). \tag{16}$$

Here, $\nabla_\perp V_{z,m}(\mathbf{r}_b)$ is shorthand for the witness-coordinate gradient specified in Eq. (15), evaluated on the common trajectory. Thus, the transverse Lorentz voltage is determined by the transverse gradient of the synchronous longitudinal voltage on that trajectory.

Summing over modes gives

$$W_\parallel(\mathbf{r}_b; s) = \sum_m K_{\parallel,m}(\mathbf{r}_b)\exp(-\alpha_m s)\cos(k_m s), \qquad s > 0, \tag{17}$$

and

$$W_s(\mathbf{r}_b; s) = \sum_m K_{s,m}(\mathbf{r}_b) \exp(-\alpha_m s) \sin(k_m s), \qquad s > 0. \tag{18}$$

The exact local derivative of Eq. (18) is

$$D_s(\mathbf{r}_b; s_0) = \sum_m K_{s,m}(\mathbf{r}_b) \exp(-\alpha_m s_0)[k_m \cos(k_m s_0) - \alpha_m \sin(k_m s_0)]. \tag{19}$$

For weak damping over the drive-witness delay, $\alpha_m s_0 \ll 1$, this reduces to

$$D_s(\mathbf{r}_b; s_0) \simeq \sum_m k_m K_{s,m}(\mathbf{r}_b) \cos(k_m s_0). \tag{20}$$

The condition $\alpha_m s_0 \ll 1$ is equivalent to

$$Q_m \gg \frac{\omega_m s_0}{2c}. \tag{21}$$

Equations (10) and (13) give the central design criterion. A mode contributes efficiently to the passive deflection only if it has strong longitudinal coupling to the common beam trajectory and strong transverse Lorentz voltage, or equivalently a strong transverse gradient of the synchronous longitudinal voltage on that trajectory. This is in contrast to an active rf transverse deflecting structure, where the external rf system directly excites the design deflecting mode. In the beam-driven case, an off-axis bunch can couple efficiently to modes whose closed-cavity parents are not dipole deflecting modes. TM-like modes contribute significantly when their longitudinal voltage is large on the common trajectory and varies strongly in the selected streaking direction. The useful streaking slope is determined by the coherent modal sum in Eq. (19), or by Eq. (20) in the weak-damping limit.

A. Mode selectivity

The drive bunch excites a spectrum of modes whose relative amplitudes depend on the longitudinal electric field E_z sampled along its path through the offset beam tube. The closed-pillbox model identifies which TM families combine strong drive coupling with a strong magnetic kick to the witness. While final numerical optimization targets the streaking slope of the combined wake, the pillbox geometry and beam-tube offset can be chosen to favor selected mode families as the dominant contributors to the transverse kick.

For a closed pillbox of radius R and length L_c, the TM parent frequencies are

$$f_{mnq} = \frac{c}{2\pi} \sqrt{\left(\frac{\chi_{mn}}{R}\right)^2 + \left(\frac{q\pi}{L_c}\right)^2}, \tag{22}$$

where χ_{mn} is the nth zero of J_m and q is the axial index.

For a mode with

$$E_{z,mnq} = E_0 J_m\left(\chi_{mn}\frac{r}{R}\right)\mathcal{C}_{m\mu}(\theta) Z_q(z), \tag{23}$$

where μ labels the two angular polarizations for $m > 0$, Maxwell's equations give

$$\mathbf{H}_{\perp,mnq} \propto \hat{\mathbf{z}} \times \nabla_\perp E_{z,mnq}. \tag{24}$$

Consequently,

$$\hat{\mathbf{z}} \times \mathbf{B}_{\perp,mnq} \propto -\nabla_\perp E_{z,mnq},$$

up to a mode-dependent normalization and phase. The magnetic part of the transverse Lorentz force is governed by the transverse gradient of the same E_z field that excites the mode.

Let

$$\Phi_{mn\mu}(r,\theta) = J_m\left(\chi_{mn}\frac{r}{R}\right)\mathcal{C}_{m\mu}(\theta) \tag{25}$$

denote the transverse dependence of the parent longitudinal field. The magnetic contribution to the drive-witness overlap scales as

$$\mathcal{G}^{(B)}_{s,mn\mu}(\mathbf{r}_s, \mathbf{r}_w) = \frac{2-\delta_{m0}}{R^2 J^2_{m+1}(\chi_{mn})} \Phi_{mn\mu}(\mathbf{r}_s)[-\mathbf{e}_s \cdot \nabla_\perp \Phi_{mn\mu}(\mathbf{r}_w)]. \tag{26}$$

The first factor is the longitudinal drive coupling; the second is the magnetic Lorentz kick projected onto the streaking direction. In the collinear geometry, $\mathbf{r}_s = \mathbf{r}_w = \boldsymbol{\rho}$.

For radial scaling estimates, one may suppress the angular factor and keep only the dependence on $u = \chi_{mn}\rho/R$. The overlap then contains the Bessel product

$$\mathcal{G}^{(B)}_{mn} \propto (2-\delta_{m0}) \frac{\chi_{mn} J_m(u) J'_m(u)}{R^3 J^2_{m+1}(\chi_{mn})}, \quad u = \chi_{mn}\frac{\rho}{R}. \tag{27}$$

The corresponding parent-mode estimate for the wake amplitude is

$$A_{mnq} \propto \mathcal{G}^{(B)}_{mn} |T_q(\omega_{mnq})|^2 F_{mnq}, \tag{28}$$

where T_q is the longitudinal transit factor and F_{mnq} is the drive bunch form factor.

The first maxima of $|J_m(u)J'_m(u)|$ for the lowest radial families are listed in Table I. The offset ratio can therefore bias the coupling toward different TM modes.

TABLE I. First maxima of the radial parent-mode product $|J_m(u)J'_m(u)|$, with $u = \chi_{m1}\rho/R$.

Angular order m	$u_{\max}$	$(\rho/R)_{\max}$
0	1.08	0.450
1	0.91	0.238
2	2.06	0.402
3	3.15	0.493

For the monopole parent modes,

$$J_0(u)J'_0(u) = -J_0(u)J_1(u), \tag{29}$$

and the first maximum occurs near

$$u \simeq 1.08, \qquad \left(\frac{\rho}{R}\right)_{\max} \simeq \frac{1.08}{\chi_{01}} \simeq 0.45. \tag{30}$$

For example, an off-axis TM_{010}-like mode, commonly used as the accelerating mode, has large longitudinal drive voltage and a nonzero radial magnetic field at the witness trajectory. It can therefore contribute to a transverse streaking wake.

Near the cavity axis,

$$J_0(u)J'_0(u) \simeq -\frac{u}{2}, \qquad J_m(u)J'_m(u) \sim u^{2m-1}\ (m \geq 1). \tag{31}$$

The monopole and $m = 1$ TM modes therefore turn on linearly with offset, whereas higher angular orders are suppressed at small ρ/R.

B. Beam-pipe aperture and modal bandwidth

The beam-pipe aperture is a primary design constraint. For a circular pipe of radius $a = d_{\text{pipe}}/2$, the lowest dipole-like cutoff is

$$f_{c,\text{TE}_{11}} = \frac{1.84118c}{2\pi a}, \tag{32}$$

and the first monopole TM cutoff is

$$f_{c,\text{TM}_{01}} = \frac{2.40483c}{2\pi a}. \tag{33}$$

A smaller beam pipe raises these cutoff frequencies and can confine a larger set of high-frequency TM-like components. Such components can increase the available streaking slope through the factor k_m in the local derivative, provided that they are not strongly suppressed by the drive-bunch form factor and that their phases remain useful at the witness delay. In contrast, accelerator operation favors a larger aperture for beam transport, alignment tolerance, and reduced sensitivity to orbit offsets.

TABLE II. Geometric parameters of the optimized 5-cell off-axis pillbox structure.

Parameter	Symbol	Value
Pillbox radius	R	9.38 mm
Cell length	L_c	3.59 mm
Period	P	4.42 mm
Beam-pipe diameter	d_{pipe}	3.01 mm
Pipe offset	ρ	2.48 mm
Active-cell fill factor	L_c/P	0.81
Offset ratio	ρ/R	0.265

III. OPTIMIZED MULTICELL STRUCTURE AND MODAL EVIDENCE

The geometry analyzed below was obtained by genetic algorithm optimization of the off-axis pillbox parameters. The objective function was the magnitude of the spatial transverse-wake derivative at one 1.3 GHz rf-bucket separation,

$$\mathcal{F}_{\text{opt}} = \left|\frac{dW_y}{ds}\right|_{s=s_{\text{rf}}}, \qquad s_{\text{rf}} = \frac{c}{1.3\ \text{GHz}} = 230.6\ \text{mm}. \tag{34}$$

The electromagnetic simulations were performed with CST Studio Suite [24]. The time-domain wakefield calculations use the finite-integration technique [25] and were used for the optimization, cell-number scaling, tolerance scans, and orbit-offset studies. The harmonic amplitudes and phases used in the decomposition were obtained from the time-domain wake potential. The mode classification is assigned by comparison with closed-pillbox analytic frequency estimates and eigenmode field patterns for the same optimized geometry. The optimized geometric parameters of the 5-cell model are listed in Table II. The resulting wake has a zero crossing close to the target delay. To compare structures of different length, we use the temporal slope per cell, $S_{\text{cell}} = S_y/N$, evaluated at the selected zero crossing. Figure 2 compares the 5-cell and 56-cell wakes after dividing each wake by its number of cells. The close agreement supports approximately linear scaling of the temporal slope with cell number over the simulated range. The small residual difference between the per-cell wakes may reflect finite-length effects and remaining numerical uncertainty in the wake calculation. A mesh convergence study showed a weak numerical-dispersion shift at moderate mesh resolution, which was reduced by increasing the mesh density.

For $d_{\text{pipe}} = 3.01$ mm, Eqs. (32) and (33) give $f_{c,\text{TE}_{11}} = 58.4$ GHz and $f_{c,\text{TM}_{01}} = 76.3$ GHz. The closed-pillbox frequency estimates for pillbox radius $R = 9.38$ mm are $f_{010} \simeq 12.2$ GHz, $f_{110} \simeq 19.5$ GHz, and $f_{210} \simeq 26.1$ GHz. The 3 mm-class beam pipe was chosen for reliable beam

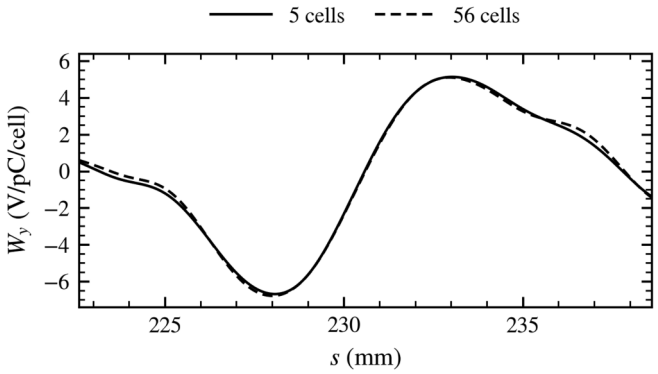


FIG. 2. Transverse wake potential per cell for the 5-cell and 56-cell structures, shown near the selected zero crossing $s_0 = 230.6$ mm. The wake potentials are divided by the corresponding number of cells before plotting, giving the ordinate in V/(pC cell). The close agreement of the two traces indicates approximately linear scaling of the transverse wake with the number of cells over this simulated range.

transport and alignment margin in the low-energy European XFEL section. The drive bunch has an rms length $\sigma_z = 80$ μm. For this bunch length, the Gaussian form factor is close to unity over the resolved modal spectrum: it is $F = 0.9841$ at 106.68 GHz. The mode damping due to lossy copper ($\sigma_{\mathrm{Cu}} = 5.8 \times 10^7$ S/m) is included in the time-domain wake calculation and in the eigenmode analysis and optimization. For the dominant eigenmodes of the optimized cell, the perturbative wall-loss quality factors are $Q_m \simeq 4.4 \times 10^3$–$6.7 \times 10^3$ over 12 GHz $\leq f_m \leq$ 28 GHz. At $s_0 = 230.596$ mm, this corresponds to $\exp(-\alpha_m s_0) = 0.993 - 0.989$, so wall-loss damping changes these modal amplitudes by only 0.7%–1.1% over the witness delay, or one linac rf-bucket spacing.

The optimized offset ratio, $\rho/R = 0.265$, lies closest to the first maximum of the $m = 1$ TM parent mode in Table I. It is well below the monopole maximum near $\rho/R \simeq 0.45$ and below the $m = 2$ maximum near $\rho/R \simeq 0.40$. Compared with the geometry of Ref. [11], which had $\rho/R \simeq 0.4$, the parent-mode scaling therefore predicts a weaker TM_{010}-like contribution and a stronger role for TM-like modes dominated by the $m = 1$ parent family. In the finite off-axis structure, the displaced beam pipe breaks cylindrical symmetry, so the simulated modes are generally mixtures of several closed-pillbox parent families rather than pure m modes.

The optimized wake has a useful zero crossing near one rf-bucket spacing,

$$s_0 \simeq 230.6 \text{ mm}. \tag{35}$$

A local linear fit to the simulated 5-cell wake $W_y(s)$ around this zero crossing, converted according to $S_y = c\, dW_y/ds$, gives

$$S_y(s_0) = 5.931 \text{ mV/(pC fs)}.$$

The temporal slope per cell is defined as

$$S_{\mathrm{cell}}(s_0; N) = \frac{S_y(s_0; N)}{N}. \tag{36}$$

For the optimized geometry, $S_{\mathrm{cell}} = 1.186$ mV/(pC fs cell).

For a structure with N coherently contributing cells, let u_s denote the screen coordinate in the selected streaking plane. The corresponding streaking factor is

$$\frac{du_s}{dt} = R_s \frac{q_d}{E_w} N S_{\mathrm{cell}}, \tag{37}$$

where q_d is the drive-bunch charge expressed in the same charge unit used for the wake normalization, E_w is the witness-beam energy in electron-volts and R_s is the transfer matrix element from the structure to the screen in the streaking plane ($R_s = R_{12}$ and $R_s = R_{34}$ for horizontal and vertical streaking respectively). For the quoted S_{cell}, q_d is therefore given in pC. With E_w expressed in electron-volts and the wake voltage in volts, the transverse voltage divided by E_w gives the dimensionless kick angle. The corresponding rms temporal resolution is

$$\sigma_{t,\mathrm{res}} = \frac{E_w\, \sigma_{u_s,0}}{|R_s| q_d\, N |S_{\mathrm{cell}}|}, \tag{38}$$

with $\sigma_{u_s,0}$ the unstreaked rms beam size on the screen in the diagnostic plane.

The resolved harmonic content of the optimized 5-cell wake is shown in Fig. 3 and detailed in Table III. The harmonic content is consistent with a periodic eigenmode interpretation. Floquet eigenmodes of a single period can be used to reconstruct the finite-structure response by weighting the modes with the appropriate phase advance and finite-cell coherence factor. For the geometry considered in Ref. [11], this reconstruction was evaluated from finite multicell eigenmode data and showed good agreement with the direct time-domain wake calculation. For optimization, the time-domain wake calculation is the most direct approach because the resulting wake potential already contains the coherent sum of the relevant modal contributions.

IV. SENSITIVITY ANALYSIS

Mechanical errors were modeled for an approximately 250-mm-long structure (56 cells) by applying uncorrelated Gaussian cell-to-cell perturbations with moderate rms amplitude of 10 μm. Ten random seeds were simulated. For each seed, the nearest zero crossing to the nominal witness delay was found and the local slope was evaluated at that crossing. Figure 4 shows a sample-mean slope

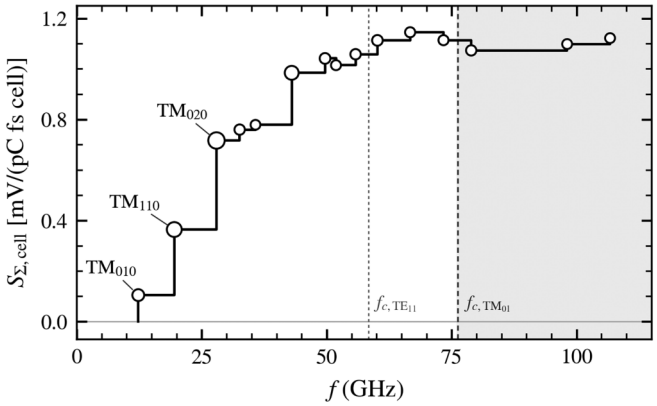


FIG. 3. Wake-only harmonic decomposition of the local temporal transverse-wake slope for the nominal 5-cell structure. The staircase shows the cumulative resolved per-cell contribution $S_{\Sigma,\mathrm{cell}}(f) = \sum_{f_i \le f} S_{i,\mathrm{cell}}$ at the witness zero crossing. Marker area is proportional to the absolute individual contribution $|S_{i,\mathrm{cell}}|$. The vertical lines mark the TE_{11} and TM_{01} circular beam pipe cutoffs. The shaded region denotes frequencies above the TM_{01} cutoff. The mode labels indicate the closest ideal closed-pillbox TM parent families.

TABLE III. Wake-derived modal contributions to the local temporal streaking slope at the zero crossing. The decomposition is normalized per cell. Parent-mode labels denote ideal closed-pillbox modes.

f_i (GHz)	Parent family	$S_{i,\mathrm{cell}}$ [mV/(pC fs cell)]	$S_{i,\mathrm{cell}}/S_{\mathrm{cell}}$ (%)
27.946	TM_{020}-like	+0.323	27.2
19.499	TM_{110}-like	+0.246	20.8
42.999	TM_{220}-like	+0.215	18.1
12.291	TM_{010}-like	+0.106	8.9
26.027	TM_{210}-like	+0.101	8.5
49.649	TM_{320}-like	+0.060	5.1
60.178	TM_{040}-like	+0.040	3.4
55.751	TM_{420}-like	+0.042	3.6
78.914	TM_{331}-like	−0.037	−3.1
73.286	TM_{430}-like	−0.024	−2.1
…	Other resolved components	+0.087	7.3
…	Unresolved residual	+0.028	2.4
…	Total	+1.186	100.0

reduction of 5.5% with a standard deviation of 2.1%. The zero-crossing shift has a sample mean of +33 μm and a standard deviation of 39 μm, with all tested cases remaining within about 110 μm of the nominal crossing. This level of phase shift requires beam-based calibration of the operating phase. However, the tested cell-to-cell perturbations do not eliminate the operating zero crossing or the local slope.

The orbit sensitivity was evaluated by varying the drive and witness trajectories in the vertical plane using the 5-cell model. For each case, the zero crossing s_0 closest to the nominal witness position was found by linear interpolation and the local slope was extracted from a local linear fit to $W_y(s)$ around that crossing. Figure 5 summarizes the resulting shift of the zero crossing and the corresponding change in streaking strength.

For the tested ±100 μm vertical offsets, the local temporal slope changes by less than about 6%. The zero-crossing position is more sensitive, with shifts up to about 30 μm. With the sign convention used in the simulations, negative vertical offset moves the trajectory toward the pillbox axis. The tested opposite horizontal split $(x_d, x_w) = (-100\ \mu\mathrm{m}, +100\ \mu\mathrm{m})$ changes the vertical wake negligibly, with $\Delta s_0 = -1.0$ μm and $\Delta S_y/S_y = -0.02\%$.

V. TUNING

A. Temperature

Uniform scaling of the copper geometry was used to estimate the sensitivity of the wake phase to structure temperature. The model assumes homogeneous thermal expansion and does not include thermal gradients or cooling-channel geometry. For copper, the scale factor is

$$\lambda_T = 1 + \alpha_{\mathrm{Cu}} \Delta T, \qquad \alpha_{\mathrm{Cu}} = 16.5 \times 10^{-6}\ \mathrm{K}^{-1}. \tag{39}$$

Thus, $\Delta T = \pm 10\,^{\circ}\mathrm{C}$ corresponds to $\lambda_T = 0.999835$ and $\lambda_T = 1.000165$. The scaled geometries were compared with a reference case at $\lambda_T = 1$.

The result is shown in Fig. 6. The zero crossing shifts approximately linearly with temperature:

$$\Delta s_0(-10\,^{\circ}\mathrm{C}) = -36.1\ \mu\mathrm{m}, \quad \Delta s_0(+10\,^{\circ}\mathrm{C}) = +38.6\ \mu\mathrm{m}.$$

In contrast, the local streaking strength remains essentially unchanged: the relative changes of S_{cell} are −0.18% and +0.03%. Therefore, uniform thermal scaling mainly shifts the witness phase while preserving the local wake slope over the tested ±10 °C range.

B. Collinear orbit offset

A controlled collinear orbit offset provides a second phase-tuning mechanism. We extend the study to collinear drive-witness offsets over the range $-300\ \mu\mathrm{m} \le y \le 300\ \mu\mathrm{m}$.

Figure 7 shows the effect of a common collinear displacement of the drive and witness trajectories. The nominal case is defined by $y = 0$, for which

$$s_0 \simeq 230.6\ \mathrm{mm}, \qquad S_{\mathrm{cell}} = 1.186\ \mathrm{mV/(pC\,fs\,cell)}.$$

Over the tested range $-0.3\ \mathrm{mm} \le y \le 0.3\ \mathrm{mm}$, the zero crossing shifts monotonically from +110 μm to −77 μm

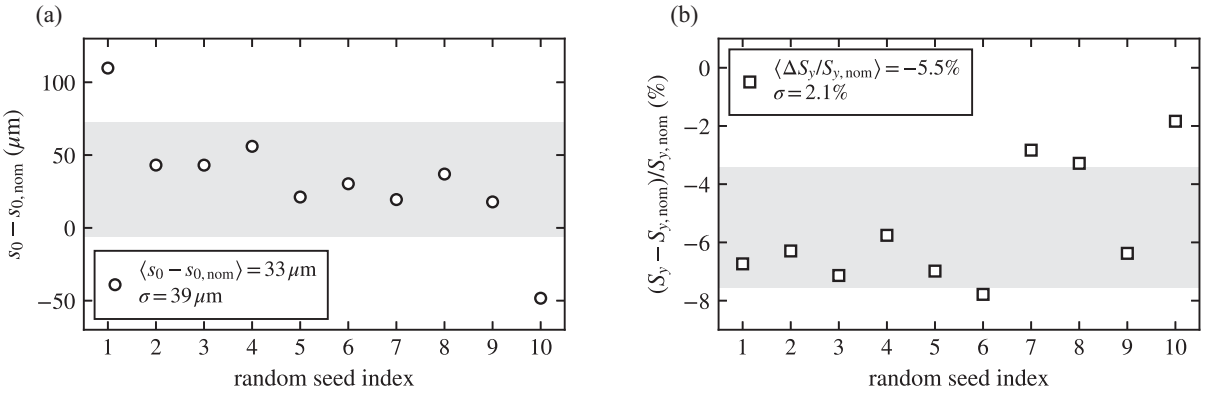


FIG. 4. Mechanical-error sensitivity of the transverse wake zero crossing. Ten independently seeded structures were generated with uncorrelated Gaussian cell-to-cell perturbations of rms amplitude 10 μm. (a) Shift of the nearest transverse-wake zero crossing after translating the longitudinal coordinate so that the nominal error-free structure is aligned to the design witness delay. (b) Relative change of the local streaking slope evaluated at each case's own zero crossing. Shaded bands indicate the mean $\pm 1\sigma$.

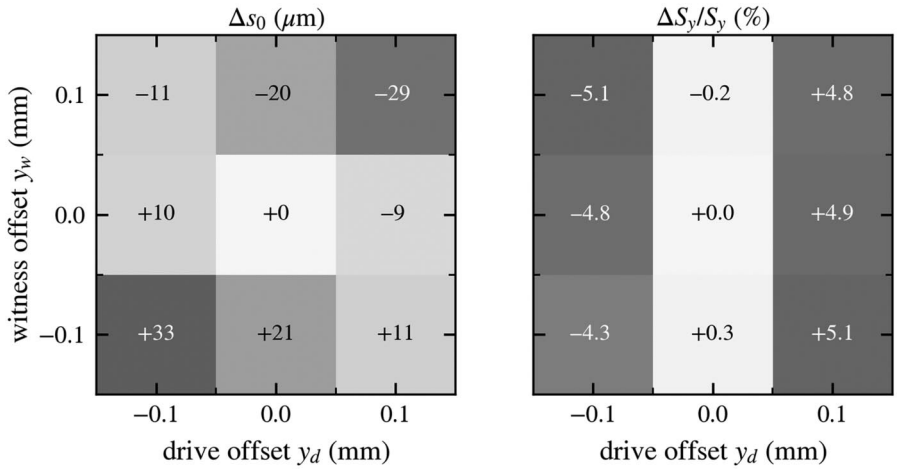


FIG. 5. Sensitivity of the transverse-wake zero crossing and local temporal slope to independent vertical orbit offsets. The horizontal axis is the drive-bunch offset and the vertical axis is the witness-bunch offset, both given as offsets from the nominal trajectory. The left panel shows the shift of the zero crossing s_0, while the right panel shows the relative change of the local slope.

relative to the nominal case. With the present sign convention, negative y moves the trajectory toward the pillbox axis. The same scan changes the per-cell temporal slope by -12% to $+16\%$ relative to nominal, corresponding to absolute values from 1.049 mV/(pC fs cell) to 1.384 mV/(pC fs cell).

C. Movable parts

Unlike conventional high-power rf resonators, a passive resonant deflector does not require rf contact between two halves of the structure. In addition to simplified production and cleaning, this can be interpreted as an additional tuning mechanism. The acceptance of the split gap is explained by the surface-current topology of the dominant TM-like modes. On the cylindrical wall of a pillbox-like TM mode, the azimuthal magnetic field produces an axial surface current,

$$\mathbf{K}_s = \hat{\mathbf{r}} \times H_\phi \hat{\boldsymbol{\phi}} = H_\phi \hat{\mathbf{z}}.$$

For a longitudinal structure split, this current flows along the seam. The gap therefore acts as a controlled perturbation of the eigenmode spectrum.

The split-block geometry is shown in Fig. 8. A gap of width g is introduced between the two copper halves in the x direction. Figure 9 shows the resulting change of the wake operating point. For 10 μm $\leq g \leq$ 100 μm, the zero crossing $s_0(g)$ shifts monotonically to larger drive-witness separation. Relative to the closed geometry, the shift reaches approximately 0.78 mm at $g = 100$ μm.

The local temporal slope was evaluated at the zero crossing corresponding to each gap. Over the same range, $S_{\mathrm{cell}}(g)$ changes moderately: it is nearly unchanged at $g = 10$ μm and is reduced by about 9.5% at $g = 100$ μm. The wake traces in Fig. 9(c) show that this perturbation

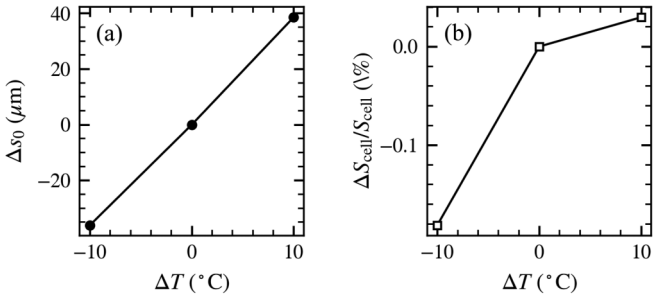


FIG. 6. Uniform thermal-scaling sensitivity of the wake operating point. Panel (a) shows the shift of the zero crossing relative to the reference geometry $\lambda_T = 1$. Panel (b) shows the relative change of the per-cell temporal slope $S_{\rm cell}$. The scaled cases assume $\lambda_T = 1 + \alpha_{\rm Cu}\Delta T$, with $\alpha_{\rm Cu} = 16.5 \times 10^{-6}$ K^{-1}.

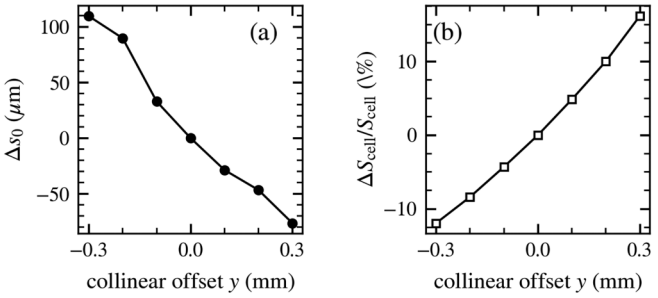


FIG. 7. Collinear orbit-offset dependence of the transverse wake. The drive and witness trajectories are displaced together with respect to the nominal beam-tube axis. Panel (a) shows the zero-crossing shift $\Delta s_0 = s_0(y) - s_0(0)$. Panel (b) shows the corresponding relative change of the per-cell temporal slope $S_{\rm cell}$.

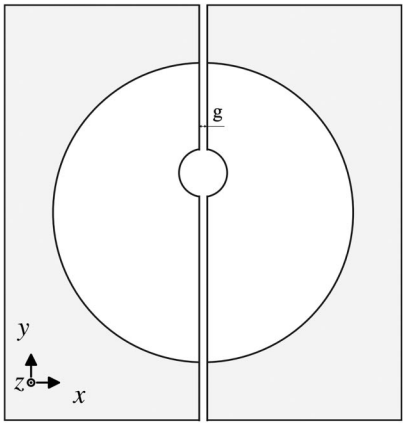


FIG. 8. Schematic x-y cross section of the split-block off-axis pillbox structure. The beam-pipe aperture is displaced in y with respect to the pillbox axis and the beam direction z.

mainly changes the phase of the wake packet. The zero crossing is displaced in s, while the local linear region used for streaking is retained over the tested gap range. An additional scan up to $g = 500$ μm gives the same sign of the phase shift, but no longer belongs to the small-perturbation regime. The zero crossing then shifts by millimeters, and the local slope decreases accordingly.

VI. EUROPEAN XFEL LOW-ENERGY USE CASE EXAMPLE

The optimized wake was applied to a longitudinal phase-space diagnostic example in the European XFEL [26] after the second bunch compressor in the three-bunch-compressor layout. The beam optics determine the screen calibration and the resolution through Eq. (38). Here, we use a witness energy $E_w = 700$ MeV, drive charge $q_d = 250$ pC, and horizontal transfer element $R_{12} = -38.73$ m from the structure to the observation screen. For this particle tracking example, the same structure is rotated so that the selected streaking plane is horizontal, with $u_s = x$, $R_s = R_{12}$, and $\sigma_{u_s,0} = \sigma_{x,0}$. Tracking without streaking gives an unstreaked horizontal rms beam size $\sigma_{x,0} = 122.2$ μm.

The nominal 5-cell wake gives a per-cell streaking strength

$$S_{\rm cell} = 1.186\ {\rm mV/(pC\,fs\,cell)}.$$

Using the period $P = 4.42$ mm, a structure of length $L = 1$ m contains $N = L/P = 226$ cells. The corresponding temporal slope is

$$NS_{\rm cell} \simeq 0.27\ {\rm V/(pC\,fs)}.$$

Inserting this value into Eq. (38) gives

$$\sigma_{t,\rm res} \simeq 33\ {\rm fs}, \tag{40}$$

for the B1 optics and the tracked unstreaked beam size.

Tracking simulations were then performed for 0.5-m-, 1.0-m-, 1.5-m-, and 2-m-long deflecting structures (see Fig. 10). The wakefields were applied as external kicks and energy changes: the long-range transverse and longitudinal wakefields were driven by the 250 pC drive bunch, and the longitudinal self-wake of the witness bunch was included separately. For a 1 m structure, the longitudinal long-range wake from the drive bunch and the longitudinal short-range self-wake of the witness bunch each produce an energy modulation of order 2 MeV, corresponding to a few 10^{-3} of the 700 MeV witness energy. The transverse streak is produced by the drive-bunch-induced transverse wake. The longitudinal wakes change the witness energy distribution and are relevant for the final screen image when the observation optics is dispersive. Their deterministic contribution can be included, in principle, in the image analysis or corrected during reconstruction.

The simulated screen separation increases with structure length, as expected from the approximately constant per-cell slope. For the present 3 mm-class aperture, the 1 m case gives an estimated temporal resolution of about 33 fs

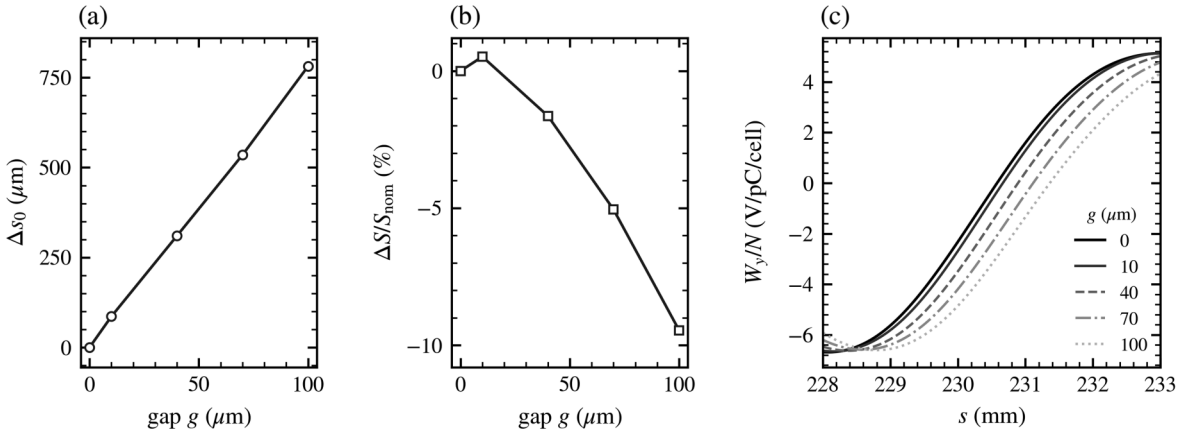


FIG. 9. Mechanical gap sensitivity of the split-block off-axis pillbox structure. (a) Shift of the transverse-wake zero crossing relative to the zero-gap nominal structure. (b) Relative change of the temporal streaking slope, $\Delta S/S_{\mathrm{nom}}$, evaluated at the corresponding zero crossing for each gap. (c) Wake potentials over the same absolute witness-delay interval.

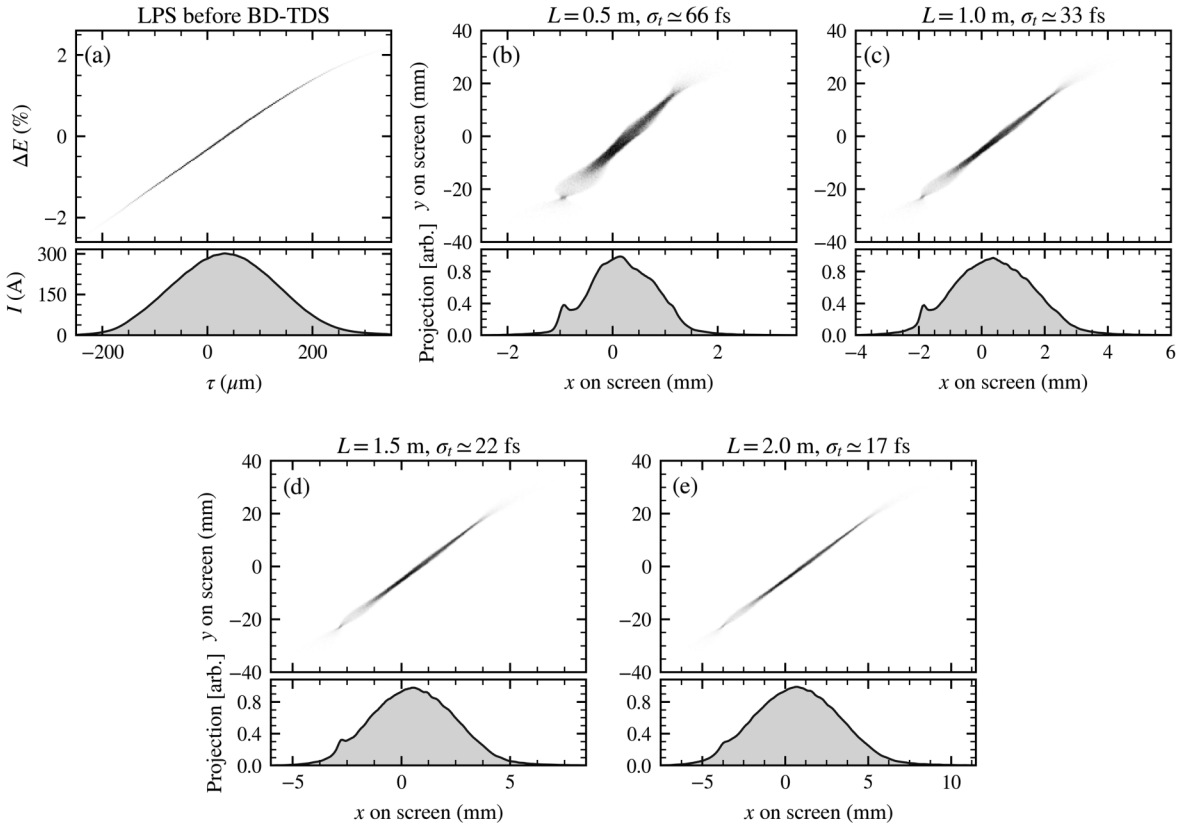


FIG. 10. Beam-dynamics example for a 3 mm-aperture beam-driven passive deflector in the B1 section. Panel (a) shows the incoming longitudinal phase space and current profile before the structure. Panels (b)–(e) show the simulated screen distributions and horizontal projections for structure lengths of 0.5 m, 1.0 m, 1.5 m, and 2 m, respectively. The particle tracking includes the drive-bunch-induced transverse and longitudinal wakes, as well as the longitudinal self-wake of the witness bunch.

for the stated optics and charge. For otherwise similar geometries, reducing the aperture is expected to increase the wake slope but reduce alignment margin.

Equal charges of 250 pC are chosen for the drive and witness bunches to simplify bunch compression and the proof-of-principle demonstration. A 500 pC drive bunch would double the streaking strength at fixed bunch profile and optics and is therefore preferable for improved temporal resolution. Simultaneous transport of the unequal-charge pair requires matching and compression

settings that accommodate their different space-charge forces and wakefields. Such common working points for 250 pC and 500 pC bunches have been obtained in European XFEL start-to-end simulations [27].

VII. CONCLUSION

We formulated a modal design framework for a beam-driven resonant passive transverse deflector and evaluated it with wake simulations. The useful operating point is a long-range transverse-wake zero crossing, and the streaking strength is characterized by the corresponding local temporal slope $S_s = c\, dW_s/ds$. The relevant modal weight is the product of drive longitudinal voltage and witness transverse Lorentz voltage, $(V_z^d)^* V_s^w/U_m$. This explains why off-axis TM-like parent families can provide a streaking wake: the drive bunch excites them through E_z, while the witness samples the transverse Lorentz force associated with the same modal fields, provided mostly by the magnetic component.

In corrugated and dielectric self-streakers, the wake builds up along the measured bunch, so its leading portion remains weakly streaked and time-resolved measurements cover only part of the bunch [13,15,16]. The preceding driver in the present scheme establishes a streak across the entire witness. This enables reconstruction of the full current profile, provided the witness fits within the linear wake region, and its transverse self-wake is negligible.

For the optimized finite structure, the 5-cell wake gives $s_0 \simeq 230.6$ mm and $S_{\mathrm{cell}} = 1.186\ \mathrm{mV/(pC\,fs\,cell)}$. The 5-cell and 56-cell comparison shows that the per-cell temporal slope is nearly unchanged over the simulated range, indicating coherent accumulation of the useful derivative. The wake-only harmonic decomposition shows that several frequency components contribute to the local slope.

The sensitivity analysis gives initial tolerance estimates for the optimized geometry. In the tested ensemble, the sample-mean slope reduction for 10 μm rms random cell perturbations is 5.5%. Independent drive-witness orbit offsets mainly shift the wake phase, while collinear orbit offsets change both phase and modal overlap. Uniform copper scaling over $\pm 10\,^{\circ}\mathrm{C}$ shifts the zero crossing by about ± 40 μm with negligible slope change in the simulated model. A longitudinal split-block gap provides a stronger phase perturbation: for $10\ \mu\mathrm{m} \le g \le 100\ \mu\mathrm{m}$, the zero crossing moves monotonically by up to 0.78 mm, while the local slope remains within about 10% of the closed-geometry value. For the European XFEL low-energy example, a 1 m structure, a 250 pC drive bunch and a 700 MeV witness beam give an estimated temporal resolution of about 33 fs.

One of the central practical conclusions is that the high-frequency multimode wake composition does not make the operating point fragile. In principle, small geometric or orbit perturbations could change the modal phases and suppress the zero-crossing derivative. The simulations show instead that the tested perturbations mainly displace the wake phase or change the modal overlap moderately, while preserving a usable local slope. The temperature, orbit, and split-gap correlations provide tuning flexibility for setting the working point together with beam-based calibration. The split-block result is especially relevant for implementation as the structure does not require an rf-tight electrical contact between the two copper halves. Water cooling can be used for temperature and phase stabilization.

A copper prototype is planned for installation and testing after the second bunch compressor in the three-bunch-compressor layout of the European XFEL. At the time of writing, discussions with manufacturers regarding its fabrication have been initiated.

DATA AVAILABILITY

There are no publicly available research data or software supporting this manuscript. Requests for further information or data should be sent to the authors.

[1] W. K. H. Panofsky and W. A. Wenzel, Some considerations concerning the transverse deflection of charged particles in radio-frequency fields, Rev. Sci. Instrum. **27**, 967 (1956).

[2] K. Floettmann and V. V. Paramonov, Beam dynamics in transverse deflecting rf structures, Phys. Rev. ST Accel. Beams **17**, 024001 (2014).

[3] M. Röhrs, C. Gerth, H. Schlarb, B. Schmidt, and P. Schmüser, Time-resolved electron beam phase space tomography at a soft X-ray free-electron laser, Phys. Rev. ST Accel. Beams **12**, 050704 (2009).

[4] Y. Ding, C. Behrens, P. Emma, J. Frisch, Z. Huang, H. Loos, P. Krejcik, and M.-H. Wang, Femtosecond X-ray pulse temporal characterization in free-electron lasers using a transverse deflector, Phys. Rev. ST Accel. Beams **14**, 120701 (2011).

[5] V. A. Dolgashev, G. Bowden, Y. Ding, P. Emma, P. Krejcik, J. Lewandowski, C. Limborg, M. Litos, J. Wang, and D. Xiang, Design and application of multi-megawatt X-band deflectors for femtosecond electron beam diagnostics, Phys. Rev. ST Accel. Beams **17**, 102801 (2014).

[6] C. Behrens, F.-J. Decker, Y. Ding, V. A. Dolgashev, J. Frisch, Z. Huang, P. Krejcik, H. Loos, A. Lutman, T. J. Maxwell, J. Turner, J. Wang, M.-H. Wang, J. Welch, and J. Wu, Few-femtosecond time-resolved measurements of X-ray free-electron lasers, Nat. Commun. **5**, 3762 (2014).

[7] P. Craievich *et al.*, Novel X-band transverse deflection structure with variable polarization, Phys. Rev. Accel. Beams **23**, 112001 (2020).

[8] B. Marchetti *et al.*, Experimental demonstration of novel beam characterization using a polarizable X-band transverse deflection structure, Sci. Rep. **11**, 3560 (2021).

[9] P. González Caminal *et al.*, Beam-based commissioning of a novel X-band transverse deflection structure with variable polarization, Phys. Rev. Accel. Beams **27**, 032801 (2024).

[10] E. Prat, Z. Geng, C. Kittel, A. Malyzhenkov, F. Marcellini, S. Reiche, T. Schietinger, and P. Craievich, Attosecond time-resolved measurements of electron and photon beams with a variable polarization X-band radiofrequency deflector at an X-ray free-electron laser, Adv. Photonics **7**, 026002 (2025).

[11] S. Tomin, D. Bazyl, W. Decking, and I. Zagorodnov, Beam-driven transverse deflecting structure for femtosecond electron-beam diagnostics, arXiv:2605.13752.

[12] K. L. F. Bane and G. Stupakov, Corrugated pipe as a beam dechirper, Nucl. Instrum. Methods Phys. Res., Sect. A **690**, 106 (2012).

[13] S. Bettoni, P. Craievich, A. A. Lutman, and M. Pedrozzi, Temporal profile measurements of relativistic electron bunch based on wakefield generation, Phys. Rev. Accel. Beams **19**, 021304 (2016).

[14] J. Seok, M. Chung, H.-S. Kang, C.-K. Min, and D. Na, Use of a corrugated beam pipe as a passive deflector for bunch length measurements, Phys. Rev. Accel. Beams **21**, 022801 (2018).

[15] P. Dijkstal, A. Malyzhenkov, P. Craievich, E. Ferrari, R. Ganter, S. Reiche, T. Schietinger, P. Juranić, and E. Prat, Self-synchronized and cost-effective time-resolved measurements at x-ray free-electron lasers with femtosecond resolution, Phys. Rev. Res. **4**, 013017 (2022).

[16] P. Dijkstal, W. Qin, and S. Tomin, Longitudinal phase space diagnostics with a nonmovable corrugated passive wakefield streaker, Phys. Rev. Accel. Beams **27**, 050702 (2024).

[17] I. Dornmair, C. B. Schroeder, K. Floettmann, B. Marchetti, and A. R. Maier, Plasma-driven ultrashort bunch diagnostics, Phys. Rev. Accel. Beams **19**, 062801 (2016).

[18] C. A. Lindstrøm, E. Adli, J. M. Allen, W. An, C. Beekman, C. I. Clarke, C. E. Clayton, S. Corde, A. Doche, J. Frederico, S. J. Gessner, S. Z. Green, M. J. Hogan, C. Joshi, M. Litos, W. Lu, K. A. Marsh, W. B. Mori, B. D. O'Shea, N. Vafaei-Najafabadi, and V. Yakimenko, Measurement of transverse wakefields induced by a misaligned positron bunch in a hollow channel plasma accelerator, Phys. Rev. Lett. **120**, 124802 (2018).

[19] V. A. Dolgashev, P. Emma, M. Dal Forno, A. Novokhatski, and S. Weathersby, Attosecond diagnostics of multi-GeV electron beams using W-band deflectors, in *Proceedings of FEIS-2: Femtosecond Electron Imaging and Spectroscopy, Lansing/East Lansing, Michigan* (2015), https://www.bmtdynamics.org/FEIS-2/talks/FEIS-2_Dolgashev.pdf.

[20] M. Dal Forno, V. Dolgashev, G. Bowden, C. Clarke, M. Hogan, D. McCormick, A. Novokhatski, B. Spataro, S. Weathersby, and S. G. Tantawi, Experimental measurements of rf breakdowns and deflecting gradients in mm-wave metallic accelerating structures, Phys. Rev. Accel. Beams **19**, 051302 (2016).

[21] A. W. Chao, *Physics of Collective Beam Instabilities in High Energy Accelerators* (Wiley, New York, 1993).

[22] B. W. Zotter and S. A. Kheifets, *Impedances and Wakes in High-Energy Particle Accelerators* (World Scientific, Singapore, 1998).

[23] G. Stupakov, Wake and impedance, Lecture notes (2018).

[24] Dassault Systèmes, CST Studio Suite: Electromagnetic field simulation software, https://www.3ds.com/products/simulia/cst-studio-suite.

[25] T. Weiland, A discretization method for the solution of Maxwell's equations for six-component fields, Electron. Commun. **31**, 116 (1977).

[26] W. Decking *et al.*, A MHz-repetition-rate hard x-ray free-electron laser driven by a superconducting linear accelerator, Nat. Photonics **14**, 391 (2020).

[27] Y. Kot, T. Limberg, and I. Zagorodnov, Two charges in the same bunch train at the European XFEL, in *Proceedings of the 36th International Free Electron Laser Conference (FEL2014), Basel, Switzerland* (2014), pp. 678–681.